The origin of magnetism in a supposedly nonmagnetic osmium oxide

S. Agrestini,[1] F. Borgatti,[2] P. Florio,[3] J. Frassineti,[4] D. Fiore Mosca,[5] Q. Faure,[6] B. Detlefs,[6] C. J. Sahle,[6] S. Francoual,[7] J. Choi,[1] M. Garcia-Fernandez,[1] K.-J. Zhou,[1] V. F. Mitrovic,[8] P. M. Woodward,[9] G. Ghiringhelli,[3] C. Franchini,[4] F. Boscherini,[4] S. Sanna,[4] and M. Moretti Sala[3]

[1]*Diamond Light Source, Harwell Campus, Didcot OX11 0DE, United Kingdom*

[2]*Istituto per lo Studio dei Materiali Nanostrutturati, Consiglio Nazionale delle Ricerche (CNR-ISMN), Via P. Gobetti 101, I-40129 Bologna, Italy*

[3]*Dipartimento di Fisica, Politecnico di Milano, Piazza Leonardo da Vinci 32, I-20133 Milano, Italy*

[4]*Dipartimento di Fisica e Astronomia, Alma Mater Studiorum - Università di Bologna, Viale C. Berti Pichat 6/2, I-40127 Bologna, Italy*

[5]*Centre de Physique Théorique, Ecole Polytechnique, CNRS, Institut Polytechnique de Paris, 91128 Palaiseau Cedex, France*

[6]*European Synchrotron Radiation Source, 71 Avenue des Martyrs, F-38000 Grenoble, France*

[7]*Deutsches Elektronen-Synchrotron DESY, Notkestr. 85, D-22607 Hamburg, Germany*

[8]*Department of Physics, Brown University, Providence, Rhode Island 02912, USA*

[9]*Department of Chemistry and Biochemistry, The Ohio State University, Columbus, Ohio 43210, USA*

(Dated: June 21, 2024)

I. EXPERIMENTAL DETAILS

A. Os L_3 edge RIXS measurements

Os L_3 edge RIXS measurements were carried out at beamline ID20 of ESRF (Grenoble, France). Monochromatic incident photons were obtained using either a Si(311) or a Si(664) channel-cut, while the energy of the scattered photon was analysed using a spherical $R = 2$ m diced Si(664) crystal; the two configurations provided a low energy-resolution (300 meV), high throughput and a high energy-resolution (60 meV), low throughput setups, respectively. More details on the RIXS spectrometer can be found in Ref. 1. The scattering geometry was horizontal, with π polarized incident photons. The scattering angle was close to 2θ=90° in order to minimize non-resonant elastic scattering. The sample was kept at ambient temperature.

B. O K edge RIXS measurements

O K edge RIXS measurements were carried out at beamline I21 of DLS (Didcot, United Kingdom) [2]. Energy- and temperature-dependent RIXS measurements were performed at normal incidence with the exit slit opening to 20 μm, corresponding to an average energy resolution of 28 meV. The scattering angle 2θ was kept fixed to 154°. Energy-dependent RIXS was performed in the 528–533 eV range (Fig. 2), to fully capture the resonance

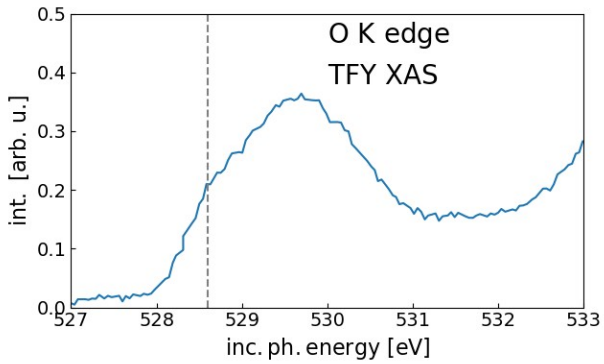

FIG. 1. O K edge XAS of Ba_2NaOsO_6 at 20 K using the total fluorescence yield mode. The vertical dotted line indicates the incident photon energy used for temperature- and momentum-dependent O K edge RIXS measurements.

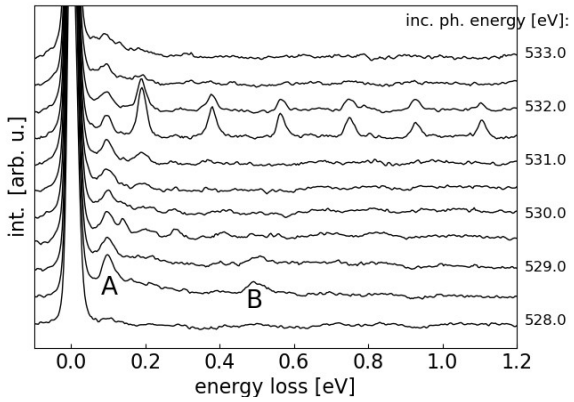

FIG. 2. O K edge RIXS spectra of Ba_2NaOsO_6 at 20 K as a function of the incident photon energy.

behaviour across the pre-edge region of the O K XAS (shown in Fig. 1). The A and B excitations in O K edge RIXS were found to resonate at a common incident photon energy around 528.5-529.0 eV, while the continuum of multi-phonon excitations extending up to 0.4 eV resonates at higher incident photon energies between 529.5 and 531.5 eV. The sharp peaks appearing for incident photon energies of 531.5 and 532.0 eV are vibrational modes of molecular water, which condensed onto the sample surface at low temperature. These peaks disappear at high temperature.

The vertical dotted line in Fig. S1 indicates the incoming photon energy used for the temperature- and momentum-dependent RIXS measurements. The momentum-dependent O K edge RIXS spectra were collected along the (h,0,0) r.l.u. direction in the reciprocal space by varying the incident angle of the incoming beam with respect to the sample surface (Fig. 3). Noteworthy, the energy positions of peaks A and B does not change with momentum transfer.

C. Os $L_{2,3}$ edge XMCD measurements and their analysis based on the use of sum rules

The XMCD measurements were carried out on beamline P09 of PETRA III at DESY (Hamburg, Germany) [3]. XMCD measurements were performed at low temperatures between 4 and 50 K in transmission mode on $Ba_2NaCaOsO_6$ powder samples by fast-switching the beam helicity between left and right circular polarization [4] and applying an external

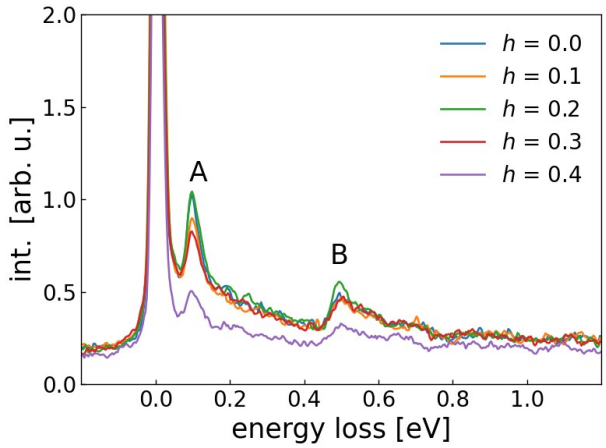

FIG. 3. O K edge RIXS spectra of Ba_2NaOsO_6 at 20 K as a function of the transferred momentum along the (h,0,0) r.l.u. direction in reciprocal space.

magnetic field of ±5 T parallel and antiparallel to the incident beam wave vector using a 6T/2T/2T vector magnet in order to align the magnetic domains and correct for nonmagnetic artifacts.

It is customary to use so-called sum rules [5, 6] to extract relevant physical quantities from XMCD data, including the expectation values of the orbital and spin angular moments. Unfortunately, the estimate of the expectation values of L and $2S$, separately, relies on the knowledge of the number of Os 5d holes, which is significantly different from the nominal because of the strong covalent nature of the Os-O bond; however, their ratio does not. Still, the estimate of $L/2S$ requires the knowledge of the expectation value of the intra-atomic magnetic dipole moment T. It can be neglected, as is usually done for transition metal ions in octahedral environment, or calculated, e.g., by means of MLFT calculations. In case T is neglected, sum rules provide an estimate for $L/2S = L/2S_{\text{eff}}$ amounting to -0.369 and confirm that i) the orbital and spin magnetic moments have opposite signs and that ii) its departure from -1 prevents the cancellation of the magnetic moment, which therefore remains finite. However, the neglect of T underestimates the $L/2S$ ratio [7–9], as we discuss below.

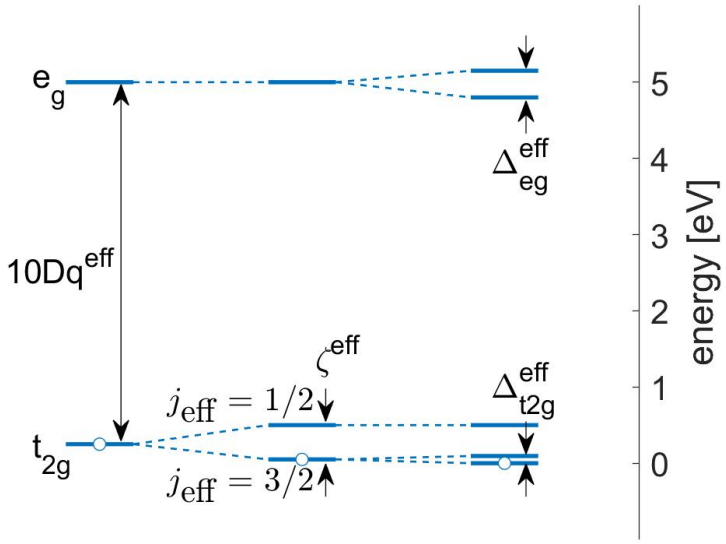

FIG. 4. Energy diagram of the Os^{7+} states from MFLT calculations. The empty circle represents the ground state of the nominal $5d^1$ configuration.

II. MULTIPLET LIGAND FIELD THEORY

Multiplet ligand field theory (MLFT) calculations were performed using Quanty [10–12]. The method uses a OsO_6 cluster, which includes explicitly the full atomic multiplet interactions (described by the Slater integrals, spin-orbit coupling λ, and U_{dd} and U_{pd}), the Os-O hybridization [$V(e_g)$ and $V(t_{2g})$], the crystal field acting on the Os ($10Dq^{ion}$, $\Delta^{ion}_{t_{2g}}$ and $\Delta^{ion}_{e_g}$) and on the ligand ($10Dq^{lig}$) states, where the latter are further offset in energy with respect to the former by the charge transfer energy (Δ_{CT}). Hybridization strengths, crystal field splittings, spin-orbit coupling and charge transfer energy have been varied to best fit the RIXS data, while Slater integrals have been fixed to 70% of the Hartree-Fock values. For all simulations we have considered the thermal population of the electronic state using the Boltzmann distribution. The parameters that best fit the experiments are (values in eV): $U_{dd} = 1.0$, $U_{pd} = 3.0$, $\Delta_{CT} = -4.0$, $\lambda = 0.41$, $10Dq^{ion} = 3.3$, $\Delta^{ion}_{t_{2g}} = -0.25$, $\Delta^{ion}_{e_g} = -0.5$, $V(e_g) = 6.2$, $V(t_{2g}) = 3.5$, $10Dq^{lig} = 0.95$.

The energies of the Os 5d states resulting from our MFLT calculations are sketched in the energy diagram of Fig. 4 and are: 0.0, 0.095, 0.5, 4.85, and 5.15 eV. They result from the simultaneous action of all the various interactions above, whose effect cannot be singled out

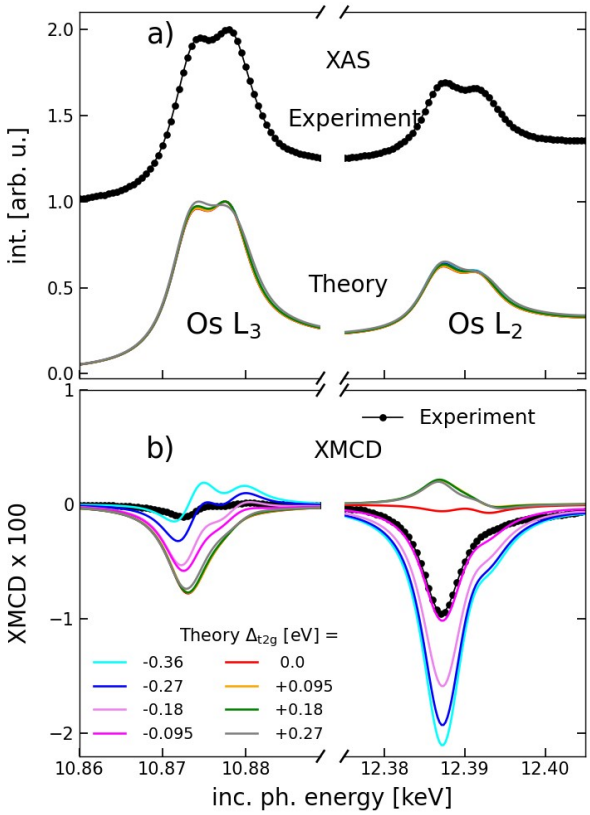

FIG. 5. Os $L_{2,3}$ edge XAS (a) and XMCD (b) spectra. The black circles and the coloured solid lines correspond to experimental and simulated curves, respectively. The simulations were performed for different values of the tetragonal crystal field splitting.

individually. Most importantly, we note that: i) hybridization splits the e_g and t_{2g} orbitals by an amount comparable to that caused by the ionic crystal field, and the two combine to produce an effective cubic crystal field splitting of $10Dq^{\text{eff}}$ = 4.9 eV; ii) covalency also partially reduces the splitting of the t_{2g} states due to spin-orbit coupling from $\zeta = 3\lambda/2$ = 0.61 eV to an effective splitting of $\zeta^{\text{eff}} = 3\lambda^{\text{eff}}/2$ = 0.49 eV; iii) tetragonal crystal field further splits the $j_{\text{eff}} = 3/2$ states by $\Delta_{t2g}^{\text{eff}}$ = -0.095 eV, as shown in Fig. S4.

A. XMCD simulations

For the simulation of the Os $L_{2,3}$ edge XAS, XMCD and RIXS spectra on a powder sample, we averaged the spectra calculated for circularly polarized light with wave vector in the xy plane and with wave vector along the z axis, with a weighting ratio of 2:1. In Fig. 5 we report

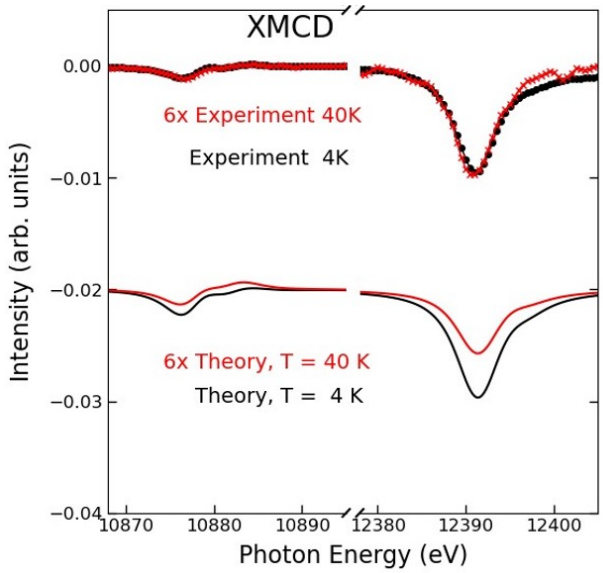

FIG. 6. Os $L_{2,3}$ edge XMCD spectra at 4 K (black) and 40 K (red). The circles and the solid lines correspond to experimental and simulated curves, respectively. The simulations were performed for $\Delta_{t2g}^{\text{eff}} = -0.095$ eV and $H_{ex} = -0.2$ meV.

simulations for the Os $L_{2,3}$ edge XAS and XCMD spectra calculated for T = 4 K and B = 5 T where the tetragonal crystal field splitting is progressively varied under the assumption that any exchange field between magnetic ions H_{ex} is absent. One can clearly see that the XMCD signal at the L_2 edge varies monotonously by going from positive (corresponding to elongated OsO_6 octahedra) to negative (compressed OsO_6 octahedra) values $\Delta_{t2g}^{\text{eff}}$. The best fit to the experimental data (dotted line) is obtained for $\Delta_{t2g}^{\text{eff}} = -0.095$ eV.

As we mentioned in the manuscript, Fig. 6 shows that the XMCD spectra at 40 K (in the paramagnetic phase) are qualitatively similar, but with reduced (approximately by a factor 6) intensity compared to the low temperature data. Since the intensity of the overall XMCD signal is directly proportional to the net magnetization of the sample, its reduction is expected in the paramagnetic phase. On the other hand, the persistent small XMCD intensity at the Os L_3 edge suggests that Os-Os interactions survive up to 40 K. MLFT calculations qualitatively account for these effects.

B. Orbital-to-spin moment ratios

The expectation values of the orbital-to-spin moment ratio ($L/2S$), magnetic moment (μ) and magnetic susceptibility (χ) within MLFT are reported in Table I. Five different scenarios (described in the first three columns of the table) were considered to clarify the role of the various interactions in determining the magnetic properties of Ba_2NaOsO_6. The values were calculated for the paramagnetic phase, i.e. at a temperature of $T = 20$ K under the assumption that any exchange field between magnetic ions H_{ex} is absent. Note that when the symmetry is lowered from O_h to D_{4h} due to a finite value of $\Delta_{t2g}^{\text{eff}}$ (0.095 eV, as extracted from O K edge RIXS and Os $L_{2,3}$ edge XMCD) the x, or equivalently y, and z axes are no longer equivalent, as evidenced by distinct values of the magnetic susceptibility in the two directions, which single out the xy plane as an easy plane of magnetization.

With the parameters reported in the last raw of Table I and $H_{\text{ex}} = -0.2$ meV, we finally calculate the average orbital $L = (L_x + L_y + L_z)/3$ and spin $2S = 2(S_x + S_y + S_z)/3$ magnetic moments, and their ratio for comparison with the value extracted by means of sum rules analysis of XMCD measurements on a powder sample at $T = 3.5$ K and $B = 5$ T. We obtain $L = -0.050\ \mu_B$, $2S = 0.090\ \mu_B$ and $L/2S = -0.551$, which is only in partial agreement with the experimental estimate of -0.369 obtained from XMCD data assuming a vanishing average intra-atomic magnetic dipole moment $T = (T_x + T_y + T_z)/3$. This difference is easily explained by MLFT calculations, which predict a non-negligible T; considering the finite value of $T = 0.006\ \mu_B$, we obtain $L/2S_{\text{eff}} = L/(2S + 7T) = -0.375$, in perfect agreement with the value extracted from XMCD data. The results of the sum rules analysis and of the MLFT calculations are summarized in Table II.

C. Magnetic susceptibility simulations

As an additional test for the parameters used in MLFT, we calculated the (inverse of the) magnetic susceptibility for a magnetic field of 2 T applied along the 100, 110 and 111 directions as a function of temperature for different values of the tetragonal crystal field $\Delta_{t2g}^{\text{eff}}$ and compared it to the corresponding experimental curves [13], as shown in Fig. 7. For the calculations, we considered the thermal population of the different energy levels according to the Boltzmann distribution. Moreover, in order to account for the dynamical (disordered)

TABLE I. Calculated orbital-to-spin moment ratio ($L/2S$), magnetic moment (μ) and magnetic susceptibility (χ) at $T = 20$ K (paramagnetic phase) and $B = 5$ T applied along the x and z directions.

			$B \parallel x$			$B \parallel z$		
site symm.	$10Dq^{eff}$ [eV]	ionic/covalent picture	$L_x/2S_x$	μ_x [μ_B]	χ_x [emu/mole/Oe]	$L_z/2S_z$	μ_z [μ_B]	χ_z [emu/mole/Oe]
O_h	∞	ionic	-1.00	0	0	-1.00	0	0
O_h	4.9	ionic	-1.92	0.007	0.8×10^{-3}	-1.92	0.007	0.8×10^{-3}
O_h	4.9	covalent	-0.66	0.004	0.4×10^{-3}	-0.66	0.004	0.4×10^{-3}
D_{4h}	4.9	ionic	-0.68	0.009	1.0×10^{-3}	-0.02	0.002	0.2×10^{-3}
D_{4h}	4.9	covalent	-0.54	0.014	1.6×10^{-3}	-0.48	0.010	1.1×10^{-3}

TABLE II. Expectation values of the average orbital (L), effective spin ($S_{\rm eff}$), intra-atomic magnetic dipole (T), spin (S) magnetic moments and their ratios as extracted from sum rules analysis of XMCD data at $T = 3.5$ K and $B = 5$ T and calculated by means of MLFT with the parameters reported in the last raw of Table I and $H_{\rm ex} = -0.2$ meV. The sum rules values have been extracted considering the nominal occupation of Os 5d states ($n_d = 1$) and the effective one ($n_d = 3.75$) obtained from MLFT calculations.

method	n_d	$1 - n_d$	L [μ_B]	$2S_{\rm eff}$ [μ_B]	$L/2S_{\rm eff}$	T [μ_B]	$2S$ [μ_B]	$L/2S$
sum rules	1	9	-0.079	0.214	-0.369	0	0.214	-0.369
sum rules	3.75	6.25	-0.055	0.149	-0.369	0	0.149	-0.369
MLFT	3.75	6.25	-0.050	0.132	-0.375	0.006	0.090	-0.551

nature of the JT distortion affecting the OsO_6 octahedra, the simulated curve for B$\|$100 was obtained by averaging over the three equivalent 100, 010 and 001 directions; the simulated curve for B$\|$110 was obtained by averaging over the six equivalent 110, 1-10, 101, 10-1, 011 and 01-1 directions; the simulated curve for B$\|$111 was obtained by averaging over the four equivalent 111, -111, 1-11 and 11-1 directions. In all cases, the simulated curve that better reproduces the experimental one is obtained for $\Delta_{t_{2g}}^{\rm eff} = -0.095$ eV, corresponding to the

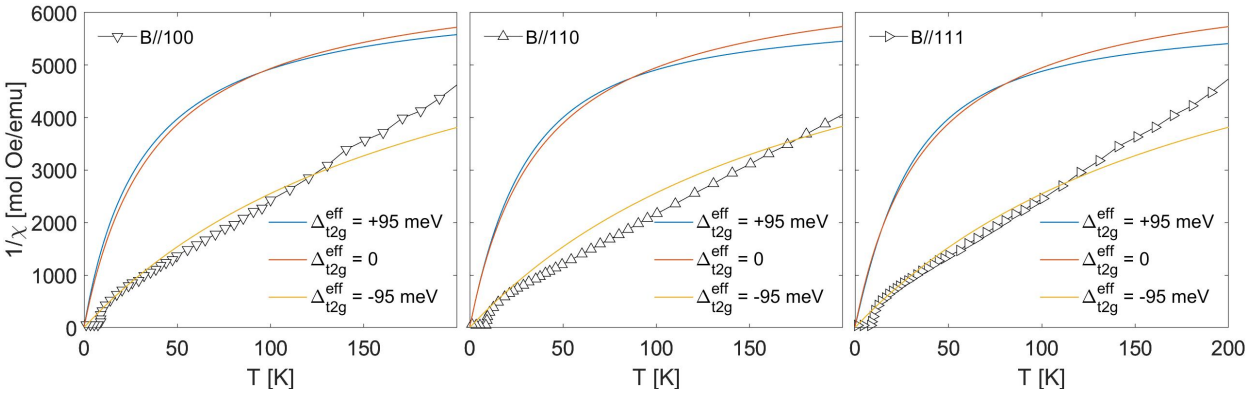

FIG. 7. Experimental (open symbols, from Ref. [13]) and simulated (continuous lines) inverse magnetic susceptibility for $Ba_2NaCaOsO_6$ as a function of temperature

case of a tetragonal compressive distortion.

[1] M. Moretti Sala, K. Martel, C. Henriquet, A. Al Zein, L. Simonelli, C. J. Sahle, H. Gonzalez, M.-C. Lagier, C. Ponchut, S. Huotari, R. Verbeni, M. Krisch, and G. Monaco, A high-energy-resolution resonant inelastic X-ray scattering spectrometer at ID20 of the European Synchrotron Radiation Facility, Journal of Synchrotron Radiation **25**, 580 (2018).

[2] K.-J. Zhou, A. Walters, M. Garcia-Fernandez, T. Rice, M. Hand, A. Nag, J. Li, S. Agrestini, P. Garland, H. Wang, S. Alcock, I. Nistea, B. Nutter, N. Rubies, G. Knap, M. Gaughran, F. Yuan, P. Chang, J. Emmins, and G. Howell, I21: an advanced high-resolution resonant inelastic X-ray scattering beamline at Diamond Light Source, Journal of Synchrotron Radiation **29**, 563 (2022).

[3] J. Strempfer, S. Francoual, D. Reuther, D. K. Shukla, A. Skaugen, H. Schulte-Schrepping, T. Kracht, and H. Franz, Resonant scattering and diffraction beamline P09 at PETRA III, Journal of Synchrotron Radiation **20**, 541 (2013).

[4] J. Strempfer, J. R. L. Mardegan, S. Francoual, L. S. I. Veiga, L. Bouchenoire, T. Spitzbart, and H. Zink, Fast helicity switching of x-ray circular polarization at beamline P09 at PETRA III, AIP Conference Proceedings **1741**, 10.1063/1.4952840 (2016), 030017.

[5] B. T. Thole, P. Carra, F. Sette, and G. van der Laan, X-ray circular dichroism as a probe of orbital magnetization, Phys. Rev. Lett. **68**, 1943 (1992).

[6] P. Carra, B. T. Thole, M. Altarelli, and X. Wang, X-ray circular dichroism and local magnetic fields, Phys. Rev. Lett. **70**, 694 (1993).

[7] C. Piamonteze, P. Miedema, and F. M. F. de Groot, Accuracy of the spin sum rule in xmcd for the transition-metal l edges from manganese to copper, Phys. Rev. B **80**, 184410 (2009).

[8] M. A. Laguna-Marco, D. Haskel, N. Souza-Neto, J. C. Lang, V. V. Krishnamurthy, S. Chikara, G. Cao, and M. van Veenendaal, Orbital magnetism and spin-orbit effects in the electronic structure of bairo$_3$, Phys. Rev. Lett. **105**, 216407 (2010).

[9] M. A. Laguna-Marco, P. Kayser, J. A. Alonso, M. J. Martínez-Lope, M. van Veenendaal, Y. Choi, and D. Haskel, Electronic structure, local magnetism, and spin-orbit effects of ir(iv)-, ir(v)-, and ir(vi)-based compounds, Phys. Rev. B **91**, 214433 (2015).

[10] M. W. Haverkort, M. Zwierzycki, and O. K. Andersen, Multiplet ligand-field theory using wannier orbitals, Phys. Rev. B **85**, 165113 (2012).

[11] Y. Lu, M. Höppner, O. Gunnarsson, and M. W. Haverkort, Efficient real-frequency solver for dynamical mean-field theory, Phys. Rev. B **90**, 085102 (2014).

[12] M. W. Haverkort, G. Sangiovanni, P. Hansmann, A. Toschi, Y. Lu, and S. Macke, Bands, resonances, edge singularities and excitons in core level spectroscopy investigated within the dynamical mean-field theory, Europhysics Letters **108**, 57004 (2014).

[13] A. S. Erickson, S. Misra, G. J. Miller, R. R. Gupta, Z. Schlesinger, W. A. Harrison, J. M. Kim, and I. R. Fisher, Ferromagnetism in the mott insulator Ba_2NaOsO_6, Phys. Rev. Lett. **99**, 016404 (2007).